Evolution of Metallicity in Vanadium Dioxide by Creation of Oxygen Vacancies

Zhen Zhang, Fan Zuo, Chenghao Wan, Aveek Dutta, Jongbum Kim, Jura Rensberg, Ronny Nawrodt, Helen Hejin Park, Thomas J. Larrabee, Xiaofei Guan, You Zhou, S. M. Prokes, Carsten Ronning, Vladimir M. Shalaev, Alexandra Boltasseva, Mikhail A. Kats, and Shriram Ramanathan

Phys. Rev. Applied **7**, 034008 — Published 10 March 2017

DOI: 10.1103/PhysRevApplied.7.034008

Evolution of Metallicity in Vanadium Dioxide by Creation of Oxygen Vacancies

Zhen Zhang,[1] Fan Zuo,[1] Chenghao Wan,[2] Aveek Dutta,[3] Jongbum Kim,[3] Jura Rensberg,[4] Ronny Nawrodt,[4] Helen Hejin Park,[5] Thomas Larrabee,[6] Xiaofei Guan,[7] You Zhou,[8] S.M. Prokes,[9] Carsten Ronning,[4] Vladimir M. Shalaev,[3] Alexandra Boltasseva,[3] Mikhail A. Kats,[2] and Shriram Ramanathan[1],*

[1]School of Materials Engineering, Purdue University, West Lafayette, IN 47907, USA,

[2]Department of Electrical and Computer Engineering, Department of Materials Science and Engineering, University of Wisconsin-Madison, Madison, WI 53706, USA

[3]School of Electrical & Computer Engineering and Birck Nanotechnology Center, Purdue University, West Lafayette, IN 47907, USA

[4]Institute for Solid State Physics, Friedrich Schiller University Jena, 07743 Jena, Germany

[5]American Society for Engineering Education (ASEE) Postdoctoral Fellow, United States Naval Research Laboratory (NRL), Washington, DC 20375, USA

[6]National Research Council (NRC) Postdoctoral Fellow, United States Naval Research Laboratory (NRL), Washington, DC 20375, USA

[7]School of Engineering and Applied Sciences, Harvard University, Cambridge, MA 02138, USA

[8]Department of Chemistry and Chemical Biology, Harvard University, Cambridge, MA 02138, USA

[9]United States Naval Research Laboratory (NRL), Washington, DC 20375, USA

*E-mail: Shriram@purdue.edu

ABSTRACT

Tuning of electronic state of correlated materials is key to their eventual use in advanced electronics and photonics. The prototypical correlated oxide VO_2 is insulating at room temperature and transforms to a metallic state when heated up to 67 °C (340 K). We report the emergence of a metallic state that is preserved down to 1.8 K by annealing thin films of VO_2 at an ultra-low oxygen partial pressure (P_{O2}~10^{-24} atm). The films can be reverted back to their original state by annealing in oxygen, and this process can be iterated multiple times. The metallic phase created by oxygen deficiency has a tetragonal rutile structure and contains a large number of oxygen vacancies far beyond the solubility at equilibrium (greater than ~50X). The oxygen starvation reduces the oxidation state of vanadium from V^{4+} to V^{3+} and leads to the metallization. The extent of resistance reduction (concurrent with tuning of optical properties) can be controlled by the time-temperature envelope of the annealing conditions since the process is diffusionally driven. This experimental platform which can extensively tune oxygen vacancies in correlated oxides provides a new approach to study emergent phases and defect-mediated adaptive electronic and structural phase boundary crossovers.

Keywords: (vanadium dioxide, metal insulator transition, defect engineering, oxygen vacancies, correlated electrons, emergent phases)

I. INTRODUCTION

Point defects and disorder strongly influence properties of correlated electron materials [1, 2]. The electronic properties of the ground state can be perturbed by several mechanisms arising from disorder, including electron donation into the conduction band from charged defects [3], and alio-valent substitutional doping and related effects [4-6]. Vanadium dioxide (VO_2) is a wellknown phase-change material that is being studied for various applications in electronics and photonics [7-10]. It is a prototypical correlated oxide system that possesses a monoclinic insulating state at room temperature, and transforms to a metallic state with a tetragonal rutile structure when heated past approximately 67 °C [11-13]. The insulating state of VO_2 at room temperature is a result of a combination of Mott and Peierls mechanisms, where the electron-electron correlations and electron-lattice coupled dimerization of vanadium ions leads to the opening of an energy gap [11, 12, 14-19]. As a result, the metal-insulator transition is very sensitive to disorder, which can alter correlation effects [20-22]. Ion irradiation experiments have shown how site disorder can modulate the metal-insulator transition [8, 23]. Substitutional defects such as W or Mo dopants, as well as interstitial defects such as hydrogen, can also dramatically modify the phase-transition temperature, and even stabilize the metallic phase down to a few Kelvin [4, 6, 20, 24]. However, these modifications are either irreversible (e.g. Mo and W dopants) [4, 6] or require catalytic electrodes coated on the surface [20].

While studies dating back over four decades have been carried out on chemical doping of VO_2, a recent topic of great interest is the emergence of metallic phases and large reversible resistance modulation in electric-double-layer thin-film transistors [25-31]. The ground state resistance of VO_2 thin films is modulated by creating oxygen-deficiency via electrochemical reactions between the VO_2 and the ionic liquid electrolyte [26, 28]. Such a metallic state is non-volatile and potentially enables applications in memory electronics, photonics, and optical metamaterials [8, 26, 31]. However, creation of oxygen-deficiency by ionic liquid gating is possibly linked with both hydrogen intercalation whence a trace of water remains in ionic liquid [29], and degradation of the entire film under high electric field [28].

Other than electrolyte gating with an ionic liquid, very few methods exist to create sufficient oxygen-deficiency to fully suppress the metal-insulator transition of VO_2 in a reversible manner. Perhaps the simplest way to introduce oxygen deficiency in VO_2 films is to reduce the oxygen content during high-temperature synthesis [32, 33]. For phase-pure oxygen-deficient $VO_{2-\delta}$ (δ is the value of oxygen deficiency) thin films, a suppression of the metal-insulator transition temperature has been observed by about 15 ^{o}C [32]. However, further reducing the oxygen content during high-temperature synthesis encounters the formation of Magnéli phases V_nO_{2n-1} ($3 \leq n \leq 8$) [32, 34] with lower oxygen stoichiometric ratios than VO_2 [35], which then prevents the creation of oxygen-deficiency in VO_2 within a single phase over a broad range. Low-temperature (450 ^{o}C) with low-vacuum (30 mTorr) annealing is another approach to introduce oxygen deficiency and prevent the formation of Magnéli phases [36]; however, in those studies, complete suppression of the metal-insulator transition was not observed. As a result, it is still a topic of active study whether or not disorder in anion sub-lattice (e.g. oxygen vacancies) solely can disturb and fully suppress the metal-insulator transition of vanadium dioxide.

Here we demonstrate a reversible metallization of VO_2 that does not require high-field ionic liquid gating or the use of hydrogen/protons as a dopant. Our approach uses low-temperature annealing at an ultra-low oxygen partial pressure (P_{O2}~10^{-24} atm). This environment is created by a dry oxygen gettering technique that does not rely on mixing hydrogen, water, or carbon monoxide gases, and is generally challenging to achieve in a film growth chamber. The resulting metallic state is stable down to 1.8 K, and the samples can be recovered back to their original state by annealing in oxygen at elevated temperature. We found that the emergence of the metallic state is accompanied by a substantial increase of reflectance in the mid-infrared wavelength range. In addition, the metallized state possesses a tetragonal rutile structure with an oxygen deficiency level of $VO_{2-\delta}$, $\delta \sim 0.2$, far beyond its solubility in equilibrium ($\delta \sim 0.004$) [35]. The metallization of VO_2 results from the reduction of vanadium ions from V^{4+} to V^{3+} when oxygen vacancies are introduced.

II. EXPERIMENT

A. Experimental setup to create low oxygen pressure environment and metallization of VO_2

The experimental setup for generating low oxygen partial pressures is shown in Fig. 1(a). Ultra-high purity (UHP) argon (Ar) gas is utilized as the starting gas, and is then filtered with a Mg-based oxygen trap (Appendix A) with a flow rate of 50 ml/min. When UHP Ar flows into the oxygen trap, the trace amount of O_2 reacts with the hot Mg (~450^{o}C) following the reaction: $Mg + ½ O_2 = MgO$. The MgO formed through this process is porous and thus does not prevent further reactions from taking place. As shown in Fig. 1(b), when the oxygen trap is ON, the oxygen partial pressure of the annealing system drops quickly and can reach $\sim 10^{-24}$ atm. The oxygen partial pressure in the annealing system is monitored using zirconia-based oxygen sensors (Appendix B). To prevent O_2 contamination from the outside, a water trap is utilized at the end-port of the annealing chamber. We do not need to mix hydrogen or carbon-containing gases, or fabricate electrodes/devices to achieve oxygen depletion in VO_2 films, so it is a clean way to study electronic and optical properties of oxides under oxygen deprivation.

The oxygen deprivation of VO_2 (deposited on sapphire substrate) in the annealing chamber is schematically shown in Fig. 1(c). During annealing, the sapphire substrate remains stable (Supplemental Material 1 [37]), which enables us to study the evolution of oxide films. At low oxygen partial pressure, the VO_2 phase becomes less stable than the Magnéli phases, which possess lower oxygen stoichiometric ratios (Supplemental Material 2 [37]). In our work, the VO_2

is held at low annealing temperatures (≤ 400°C) where the structural transformation to Magnéli phases is hindered kinetically (Supplemental Material 2 [37]). The combination of low oxygen partial pressure and low annealing temperature thus enables the formation of oxygen vacancies in tetragonal VO_2 [Fig. 1(c)]. The electrons generated via the oxygen deprivation reduce the vanadium ions from V^{4+} to V^{3+}. The principal chemical reactions that occur at the low oxygen partial pressure are:

$$\mathrm{O_o^x} \leftrightarrow \mathrm{v_O^{2+}} + 2e^- + \frac{1}{2}\mathrm{O_2(g)} \quad (1)$$

$$\mathrm{V^{4+}} + e^- \leftrightarrow \mathrm{V^{3+}} \quad (2),$$

where $\mathrm{O_o^x}$ stands for the oxygen normally occupied at anion site, $\mathrm{v_O^{2+}}$ stands for oxygen vacancies, V^{4+} and V^{3+} stand for vanadium ions in the pristine and oxygen-deficient state, respectively.

The appearance of V^{3+} in the system weakens the strong electron correlation and enables the non-volatile transformation from the insulating monoclinic phase to the metallic tetragonal phase, leading to metallization of the sample down to cryogenic temperatures, as shown in Fig. 1(d). This is reminiscent of the stabilization of the metallic state by introducing V^{3+} ions with Mo and W doping [4, 6].

Reversal to the insulating state can be achieved by annealing the sample in an oxygen-rich environment (e.g. pure oxygen) at elevated temperature, restoring the V^{4+} oxidization state. The sample then shows the metal-insulator transition similar to the pristine samples.

B. Synthesis of VO_2 thin films

VO_2 thin films with thickness of ~ 40 nm were grown by physical vapor deposition (PVD). A V_2O_5 target was magnetron sputtered in an Ar atmosphere on *c*-plane sapphire substrates. The substrates were cleaned with acetone and isopropanol, blow dried with Ar gas, and then transferred into the growth chamber. The base pressure of the growth chamber was kept at 8×10^{-8} Torr before deposition. During deposition, the Ar flux was set to 50 sccm with the pressure of the growth chamber at 5 mTorr. The substrate was heated up to 600 ^{o}C for the formation of VO_2 phase. The target power was set as 100 W so that the growth rate was controlled as 0.7 nm/min. The thin films were quenched to room temperature after deposition under an Ar flux of 50 sccm, at 5 mTorr, and then transferred out of the deposition system.

Comparable VO_2 thin films with thickness ~ 40 nm were grown by atomic layer deposition (ALD) on *c*-plane sapphire substrate. These samples were used primarily for the annealing experiments to study the general nature of the phase transition suppression in vanadium dioxide by oxygen deficiency independent of the specific growth technique. ALD VO_2 films were grown by a commercial Beneq TFS-200 reactor at 150 °C. The precursors for the vanadium and oxygen sources were tetrakis(ethylmethylamino)vanadium (TEMAV, $V(NEtMe)_4$, Air Liquide) and deionized H_2O, respectively, and ultra-high purity (UHP) argon was used as the carrier gas. The vanadium precursor was evaporated at 60 °C from an open boat inside a hot cell attached to the reactor chamber. The exposures times for each dose of TEMAV and H_2O were 2 and 0.2 seconds, respectively, using an ALD sequence of TEMAV dose / UHP Ar purge / H_2O / UHP Ar purge. VO_2 films grown by ALD were annealed in N_2 gas for ~ 1 hour at 480 °C, with a constant pressure of ~8 Torr, to convert from amorphous to crystalline VO_2.

C. Structural, electrical, and optical characterization

Electrical resistivity was measured with a Keithley 2635A source meter in a temperature controlled probe station. Low-temperature resistivity measurements were conducted under electrical transport mode in Physical Property Measurement System from Quantum Design. The temperature-dependent reflectance was investigated by near-normal incidence measurements using a mid-infrared (mid-IR) source attached to a Shamrock 500 monochromator. The reflected light was detected with a mercury-cadmium-telluride (MCT) detector in the temperature range between 25 °C and 100 °C. The crystal structure and lattice constant was studied by high resolution x-ray diffraction (XRD) using Panalytical MRD X'Pert Pro. X-ray photoelectron spectroscopic (XPS) analyses were carried out to investigate the changes of oxidation state of vanadium as well as to estimate the stoichiometry of samples [38]. High resolution XPS data was obtained with monochromatic x-ray (Al $K\alpha$) in vacuum of ~ 10^{-8} Torr. The XPS spectrum was calibrated with the C 1*s* peak. Raman spectra were measured at room temperature using 532 nm excitation with a power of 1 mW in a backscattering geometry (Renishaw inVia confocal Raman microscope). The visible and near-infrared optical properties of $VO_{2-\delta}$ were studied by variable angle spectroscopic ellipsometry (V-VASE, J. A. Woollam). The ellipsometry measurements were performed at three incident angles (55º, 65º and 75º) at 25 ºC and 90 ºC, for free-space wavelengths from 200 nm to 2000 nm. Complex optical refractive index values were extracted by fitting the experimental results with a thin-film model that includes the sapphire substrate, a VO_2 layer and surface roughness (Supplemental Material 3 [37]). In our model, the optical constants of VO_2 were described by a general oscillator function, which includes four Gaussian terms [39] for the insulator phase (found in pristine VO_2 at 25 °C), and one additional Drude term [40] for metallic phase (found in pristine VO_2 at 90 °C, and oxygen deficient $VO_{2-\delta}$ at both 25 °C and 90 °C). For each of the films, we fitted the thickness and optical constants, assuming that the thickness does not change significantly as a function of temperature.

III. RESULTS AND DISCUSSION

A. Evolution of metallic phase

PVD-grown VO_2 films with thickness of 40 nm were annealed at low oxygen partial pressure. The electrical resistivity of VO_2 after annealing is shown in Fig. 2(a). Pristine VO_2 shows a metal-insulator transition at $T_{\mathrm{MIT}} \sim 67\ ^{\mathrm{o}}\mathrm{C}$, with three orders of magnitude jump of electrical resistivity. The transport gap (E_g) in the insulating state, estimated from fitting the temperature-dependent resistivity with the equation $\rho \sim exp(E_g/2k_{\mathrm{B}}T)$ [41], is 0.58 eV, consistent with literature (~0.6 eV) [41]. After annealing the pristine sample at $300^{\mathrm{o}}\mathrm{C}$ for 2 hours, the high temperature electrical resistivity of sample at $100\ ^{\mathrm{o}}\mathrm{C}$ was found to be similar to that of pristine VO_2. However, with cooling, the sharp metal-insulator transition near $67\ ^{\mathrm{o}}\mathrm{C}$ vanishes. Instead, the metal-insulator transition is suppressed to $\sim 30\ ^{\mathrm{o}}\mathrm{C}$, with only a small resistivity change of ~2X. The reduction of the transition temperature and the resistivity jump can be observed more clearly by taking the derivative of the resistivity with respect to temperature, as shown in Fig. 2(b). The transport gap of the insulating state of the $300\ ^{\mathrm{o}}\mathrm{C}$-annealed sample is reduced to 0.32 eV [Fig. 2(a)]. Such a reduction is also observed in hydrogenated VO_2 prior to the full stabilization of the metallic state [20]. The extent of resistance reduction at low oxygen partial pressure can be controlled by varying the annealing conditions and film thickness (Supplemental Material 4 [37]). We achieved full stabilization of the metallic state by annealing the pristine VO_2 at $400^{\mathrm{o}}\mathrm{C}$ for 2 hours at low oxygen partial pressure. The sample retains the low electrical resistivity comparable to that of the metallic state of pristine sample down to room temperature.

The generality of metallization of VO_2 after annealing at low oxygen partial pressure was investigated by performing annealing experiments on VO_2 thin films with similar thickness (40 nm), synthesized by atomic layer deposition (ALD). The electrical resistivity of ALD-grown VO_2 after annealing at $400^{\mathrm{o}}\mathrm{C}$ for 2 hours is shown in Fig. 2(c). Similar to the PVD case, the metal-insulator transition of VO_2 is suppressed after annealing, leaving only the metallic state.

This demonstrates that the oxygen-vacancy-mediated metallic phase evolution process is independent of growth technique.

The metallic state of VO_2 after annealing at low oxygen partial pressure can be preserved for extended periods of time in ambient condition, which indicates potential relevance to practical applications (Supplemental Material 5 [37]). This is possible due to the kinetic limitation of oxygen diffusion into the whole film at low temperature. Since large amount of oxygen vacancies is introduced, the $VO_{2-\delta}$ after low oxygen partial pressure annealing is meta-stable.

The reversibility of metallized samples to the insulating state was studied by annealing in pure oxygen gas (P_{O2} ~ 1 atm) at elevated temperatures. We started from the metallized sample obtained by annealing the 40 nm PVD-grown VO_2 at 400 ^{o}C for 2 hours. This sample was then held at 300 ^{o}C in O_2 for 2, 4, and 6 hours. As Fig. 2(d) shows, the low-temperature electrical resistivity of the sample gradually increases with increasing annealing duration, and the metal-insulator transition is restored. After holding the metallized sample in O_2 for 6 hours at 300 ^{o}C, its transition temperature and resistivity value become similar to those of the pristine samples [Fig. 2(a)]. Moreover, the metallization of VO_2 at low oxygen partial pressure and the recovery back to the insulating state can be performed over multiple cycles (Supplemental Material 6 [37]). The reversibility of metallized samples under pure oxygen further suggests the oxygen deficiency created in VO_2 at low oxygen partial pressure is relevant to the emergence of the metallic state, in accordance with electrolyte gating experiments.

B. Mid-IR reflectance of metallic phase

To investigate the effect of low oxygen partial pressure annealing on the optical properties of VO_2, mid-IR reflectance of pristine and annealed (400 ^{o}C, 2 hours) samples was studied. The temperature-dependent mid-IR reflectance of pristine VO_2 during heating is shown in Fig. 3(a). At room temperature (25°C), the pristine VO_2 is in the insulating state and relatively transparent in the mid-IR region. The increase of reflectance above 11 μm results from the onset of the Reststrahlen band of the sapphire substrate [8, 42]. With increasing temperature, the reflectance increases between 2 μm and 10 μm, due to the increase of carrier density across the thermally induced metal-insulator transition. Around the transition temperature, a sharp increase of reflectance can be observed in Fig. 3(c).

After annealing at 400 °C for 2 hours, the temperature-dependent reflectance spectrum of sample changes [Figs. 3(a) vs. 3(b)]. The sample becomes highly reflective in the mid-IR region, even at room temperature, indicating its high carrier density after annealing. Upon heating, the reflectance of the annealed sample maintains a high value, and no signature of a metal-insulator transition is observed. Moreover, the reflectance of sample decreases slightly with heating [Fig. 3(c)], demonstrating a Drude-like metallic behavior [43]. Therefore, the mid-IR reflectance of the annealed sample demonstrates that the metallic state is stabilized after annealing at low oxygen partial pressure. The comparison of reflectance between the annealed sample and the pristine one above T_{MIT} [Fig. 3(c)] indicates the optical similarities in the mid-IR region between the metallic states induced by temperature and oxygen deficiency.

C. Stabilization of oxygen-deficient rutile $VO_{2-\delta}$

The crystallographic properties of the metallic phase after annealing at low oxygen partial pressure were studied. The room temperature XRD profiles of pristine PVD-grown 40 nm VO_2, before and after annealing at 400 °C for 2 hours, are shown in Figs. 4(a) and 4(b). For the pristine VO_2 thin film, $(020)_M$ and $(040)_M$ (M stands for monoclinic) diffraction peaks are observed indicating its epitaxial growth with orientation relation VO_2 (020)//Al_2O_3 (0006) [44]. After annealing, as Fig. 4(b) shows, the $(020)_M$ peak shifts to a lower diffraction angle with $2\theta = 39.4^o$, which is very close to the diffraction peak from the (200) plane of the tetragonal rutile structure ($2\theta = 39.5^o$) [45]. This shifting is similar to that of the thermally induced transformation from monoclinic to tetragonal rutile structure in VO_2. Except for the peak shifting, no new diffraction peak appears, indicating that the metallization of the thin film is not caused by the structural transformation from VO_2 to any of the Magnéli phases. Moreover, we confirm the tetragonal rutile structure of the metallized sample by observing off-axis (220) diffraction spot at tilting angle ψ=45^o (Supplemental Material 7 [37]). The lattice parameter of the metallized sample at room temperature is extracted from the off-axis diffraction scans as $a = b = 4.56$ Å; $c = 2.86$ Å, close to that of the pristine VO_2 in the high temperature rutile phase ($a = b = 4.55$ Å; $c = 2.85$ Å) [45].

To further confirm that the metallic state is not a Magnéli phase and to study the stability of the metallic state at cryogenic temperatures, we measured the electrical resistivity of 400 ^{o}C-2 hours annealed sample down to 1.8 K. Most Magnéli phases possess first-order metal-insulator transitions [46], and thus can be identified by the presence of abrupt resistivity jumps corresponding to their transition temperature T_{MIT} [46]. Figure 4(c) shows the cooling/heating resistivity curves of the annealed sample in the temperature region from 1.8 K to 373 K. The transition temperatures of Magnéli phases are also marked for comparison. Upon cooling to 1.8 K, no signature of a metal-insulator transition was observed in the annealed thin film. The combination of XRD and low-temperature transport studies thus demonstrate that the low oxygen pressure annealing primarily serves to introduce oxygen deficiency into VO_2 and stabilize the metallic rutile phase.

To study the level of oxygen deficiency in the metallized samples and its effect on the oxidation state of vanadium, X-ray photoelectron spectroscopic (XPS) analysis was performed. Figure 4(d) shows the V 2*p* core-level spectra of pristine and annealed samples. For the pristine sample, the V $2p_{3/2}$ core-level photoemission peak mainly appears at 516.6 eV, close to the literature value of the V^{4+} valence state (515.5 eV ~ 516.4 eV) [26, 38, 47]. After annealing, the V $2p_{1/2}$ core-level photoemission peak shifts towards low binding energy and the V $2p_{3/2}$ peak splits where a pronounced peak appears at lower binding energy, indicating the reduction of the vanadium ion after annealing. We confirmed such a reduction behavior by measuring three different regions of the samples. The V $2p_{3/2}$ peak with lower binding energy (515.6 eV) corresponds to the V^{3+} valence state (515.1 eV ~ 515.8 eV) [26, 38, 47]. The oxygen non-stoichiometry of the $VO_{2-\delta}$ after annealing at low oxygen pressure is then estimated to be $\delta \sim 0.08$ at 300 °C and 0.2 at 400 °C by the ratio of the effective XPS peak area of V^{3+} and V^{4+} after the Shirley background is subtracted. It was reported that in electron-doped $V_{1-x}W_xO_2$ thin film, the phase transition is suppressed to ~ 50 K when x ~ 0.09 [48], where W takes 6+ valence state [49]. Based on the charge neutrality ($V_{1-3x}^{4+}V_{2x}^{3+}W_x^{6+}O_2^{2-}$), about 0.197 electron doping per vanadium atom occurs. Assuming similar amount of electron doping is required to suppress the phase transition in $VO_{2-\delta}$ ($V_{1-2\delta}^{4+}V_{2\delta}^{3+}O_{2-\delta}^{2-}$), the critical value of δ to suppress phase transition is estimated to be 0.098, being consistent with present observations [Fig. 4(d)].

Previous work on phase equilibria in the V_2O_3-VO_2 system at 1600 K shows that the maximum concentration of oxygen vacancies in single phase $VO_{2-\delta}$ is $\delta = 0.004$, beyond which Magnéli phases form [35]. It is therefore surprising that the oxygen vacancy concentration generated by annealing can reach $\delta = 0.2$. We believe this is attributed to the extreme low oxygen partial pressure coupled with kinetic hindrance of structural degradation at the low annealing temperatures. Comparison to previous work reporting stabilization of the metallic state by electrolyte gating in VO_2 field-effect transistor indicates that this level of oxygen deficiency can also be created by electric fields in electric-double-layer transistors when the electrochemical stability window is exceeded [26, 28]. Given the high levels of non-stoichiometry, such systems could be well-suited for synchrotron studies to precisely investigate the local structure.

D. Destabilization on V-V dimerization in VO_2 due to oxygen vacancies

To further study the effect of oxygen vacancies on structural instability and V-V dimerization of VO_2 during the transition from its insulating monoclinic state to the oxygen-deficient metallic state, Raman spectra of PVD-grown 40 nm VO_2 annealed at 300 ^oC, 350 ^oC and 400 ^oC for 2 hours (i.e. increasing oxygen vacancy concentration) were investigated. As Fig. 5(a) shows, the pristine VO_2 thin film is in the monoclinic structure at room temperature with sharp Raman peaks at 129, 196, 224, 308, 386, 498, and 614 cm^{-1} for A_g symmetry, and 268, 340, and 445 cm^{-1} for B_g symmetry [50, 51]. Extra peaks at 421, 575, and 751 cm^{-1} are due to the Raman signal from the Al_2O_3 substrate. After annealing at 400 ^oC for 2 hours, all peaks corresponding to the monoclinic structure vanish. Instead, a heavily damped Raman peak appears, centered at 530 cm^{-1}. The value and shape of this damped peak are coincident with that of the A_{1g} mode of the thermally induced rutile metallic state in pristine VO_2 [50]. With increasing annealing temperature, the peak around 530 cm^{-1} corresponding to the rutile structure gradually becomes dominant, while the intensity of peaks corresponding to the monoclinic structure decreases [Fig. 5(b)], indicating the gradual reduction in the fraction of the insulating phase in the sample.

The shifting of Raman modes due to the introduction of oxygen vacancies is shown in Figs. 5(c) and 5(d). We focus on an A_g mode at 614 cm^{-1} related to V-O bonding [Fig. 5(c)] and

A_g modes at 196 and 224 cm^{-1} related to the pairing and tilting of V-V bonds [Fig. 5(d)] [52, 53]. After annealing at 400 $^{\mathrm{o}}$C for 2 hours, the peak corresponding to the V-O bonding mode at 614 cm^{-1} [Fig. 5(c)] shifts down by 10 cm^{-1}. Simultaneously, the peaks corresponding to V-V dimerization at 196 and 224 cm^{-1} [Fig. 5(d)] shift down by 1.5 cm^{-1}. As a comparison, the Raman peak at 751 cm^{-1} from the substrate does not shift. The softening of V-O and V-V mode is similar to that of the thermally induced metal-insulator transition in pristine VO_2 [52, 54], indicating the destabilization of the monoclinic structure due to oxygen deficiency. Previous work indicates that the Peierls instability, i.e. distortion of V-O octahedral and dimerization of V-V in the monoclinic state, plays an important role in opening an energy gap during the metal-insulator transition of VO_2 [11, 14]. As a result, the emergence of the metallic state after low oxygen partial pressure annealing can be understood at least partially as the result of the degradation of the Peierls mechanism with respect to oxygen deficiency and reduction of V^{4+}.

E. Optical properties of oxygen-deficient metallic state

Optical properties of the metallic state after annealing were further investigated by ellipsometry measurements. The refractive index data of a pristine PVD-grown 40 nm VO_2 film and one annealed at 400$^{\mathrm{o}}$C for 2 hours are presented in Figs. 6(a) and 6(b). For pristine VO_2 [Fig. 6(a)], a large increase of the real part of refractive index n and reduction in the extinction coefficient κ are observed in the wavelength range of 700 - 2000 nm across the metal (90 $^{\mathrm{o}}$C) to insulator (25 $^{\mathrm{o}}$C) transition [16]. Such a change is not seen in the annealed $VO_{2-\delta}$ film [Fig. 6(b)]. Moreover, the opposite temperature-dependent behavior occurs as the extinction coefficient κ of $VO_{2-\delta}$ increases slightly with cooling, demonstrating the vanishing of the metal-insulator transition that is consistent with electrical measurements [Fig. 2(a)]. The optical properties of $VO_{2-\delta}$ at both temperatures are found to be similar to that of pristine VO_2 at 90 ºC, indicating that the metallized $VO_{2-\delta}$ is closely related to the thermally induced metallic state in pristine VO_2 [43]. The real part of the optical conductivity σ_1 of the oxygen-deficient sample is calculated from the complex refractive index and compared with the thermally induced metallic state in VO_2 [the upper panel of Fig. 6(c)] [43]. It is found that both samples show Drude-like behavior with similar optical conductivity in the low photon energy region.

Another interesting feature is the significant reduction of the broad absorption peak between 2.5 and 4 eV shown in the upper panel of Fig. 6(c). For a better understanding of this reduction, the band structure of VO_2 is depicted schematically in Figs. 6(d)~6(f) based on the Goodenough model [11]. In pristine metallic VO_2 [Fig. 6(e)], this absorption peak corresponds to the interband transitions from the O_{2p} band to the π^* and $d_{//}$ bands labeled as *B* and *A*, the energy value of which is consistent with previous works [55]. The π^* and $d_{//}$ bands are overlapped and partially filled in metallic state. Upon the metal-insulator transition in pristine VO_2 [Fig. 6(d)], the $d_{//}$ band further splits due to the dimerization of vanadium ions and the π^* band shifts up, and an energy gap appears between the fully occupied lower $d_{//}$ band and the empty π^* band. Such band structure reconstruction is attributed to the combined effect of lattice-electron coupling (Peierls transition) and electron-electron correlations (Mott-Hubbard transition) [11, 12, 14-19]. The interband transition in the insulating state [Fig. 6(d)] gives rise to three peaks in its optical conductivity labeled as *C*, *D*, and *E* [Fig. 6(c) lower panel]. Under oxygen deficiency [Fig. 6(c) upper panel], the significant reduction of the two absorption peaks (*A* and *B*) compared to the metallic state of pristine VO_2 indicates the reduction of un-occupied states in the π^* and $d_{//}$ bands [Fig. 6(f)], i.e., band filling with electrons generated by the oxygen vacancies. Such a band filling effect then suppresses the metal-insulator transition [4, 20, 22, 32, 36, 56] and leads to the stabilization of metallic state.

IV. CONCLUSIONS

We have introduced an oxygen gettering approach to create low oxygen partial pressures to study correlated electron materials. Our technique allows systematic post-growth tuning of oxygen defects in a model system, vanadium dioxide (VO_2), without introducing ionic liquids, water or hydrogen and without forming Magnéli phases. We show that the oxygen deficiency level induced by this method can greatly exceed the solubility limit in equilibrium, and can be used to reversibly modify the electrical, optical, and structural properties via a defect-induced non-volatile metal-insulator transition. Disorder on the anion sub-lattice which enables structural change and charge filling synergistically is therefore an elegant approach to designing non-volatile functional properties in correlated oxides. Such materials with widely adaptive properties and environmental response hold promise in neuromorphic computing and adaptive electromagnetics.

ACKNOWLEDGEMENTS

Funding from Army Research Office and Office of Naval Research is acknowledged. This work has been partially financed by the Initiative and Networking Fund of German Helmholtz Association, Helmholtz Virtual Institute VH-VI-422 MEMRIOX. MK acknowledges support from the Office of Naval Research (N00014-16-1-2556). VS and AB acknowledges support from Air Force Office of Scientific Research MURI grant (FA9550-14-1-0389).

APPENDIX A: Mg-based oxygen trap system design and operational principle

Figure 7 shows a cross-sectional schematic of the Mg-based O_2 trap setup built for our study. Mg powder (Sigma Aldrich) was placed between ceramic insulation rolls inside a stainless-steel tube container. The stainless-steel tube was wrapped by a heating tape powered by a variable transformer (Staco Energy), and the temperature near the working zone of the O_2 trap was monitored by a thermocouple. A layer of ceramic insulation roll covered the heating tape and the stainless-steel tube container to reduce heat dissipation during heating. A piece of aluminum foil sheathed the porous ceramic insulation roll.

When Ar gas flowed into the oxygen trap setup, the trace amount of O_2 impurity reacted with the Mg following the reaction: $Mg + ½ O_2 = MgO$. The MgO formed was porous and thus did not prevent further reaction from taking place. The theoretical P_{O2} at the Mg/MgO equilibrium can be calculated from the equilibrium constant (K_{eq}) of the reaction following the equation:$P_{O2} = a_{MgO}/(a_{Mg} \cdot K_{eq})$, where $a_{MgO} = 1$ is the activity of MgO, and $a_{Mg} = 1$ is the activity of Mg. The value of K_{eq} as a function of temperature from 350 °C to 500 °C is obtained from HSC Chemistry Database [57] and shown in Table (I). Besides thermodynamic considerations, the actual P_{O2} in the Ar gas after passing through the Mg-based O_2 trap setup is strongly influenced by the kinetic factors including the reaction rate and time. Although the equilibrium P_{O2} goes down as the operation temperature decreases, the reaction rate also decreases. Therefore, the operation temperature cannot be too low and sets experimental limits. The optimum operation temperature of the Mg-based O_2 trap is typically a few hundred degrees to ensure both a low equilibrium P_{O2} and a relatively high reaction rate. In this work, we heated up the Mg to 450 ^{o}C, which enables a theoretical oxygen partial pressure about 10^{-75} atm. In experiments, the theoretical oxygen partial pressure was difficult to reach due to the constant flowing of Ar gas and the possible gas leakage near the tube fitting area. As shown in Fig. 1(b), an oxygen partial pressure, as low as 10^{-24} atm was reached in our work. In future experiments, if we can control the flow rate to lower values, it is possible to achieve even lower partial pressures.

For instance, Y. M. Chiang and co-workers have demonstrated similar solid-state buffering routes to reach 10^{-40} atm oxygen partial pressures in studies on the stability of Si-SiO$_2$ interfaces [58].

At very low partial pressure, the kinetics of oxygen molecules becomes relevant. Based on the kinetic theory of gases, the impingement rate Z, i.e., the number of molecules striking the surface perpendicular to their moving direction, per unit time, is expressed as [59]:

$$Z = \frac{P}{\sqrt{2\pi m k_B T}} = 8.333 \times 10^{22}\, P/(TM)^{\frac{1}{2}}\, (molecules/m^2 s) \qquad (3)$$

where P is pressure of gas (Pa), T is temperature (K), m is mass of gas molecules (g), M is molar mass (kg/mol), and k_B is Boltzmann constant. In our experiment, the surface area of oxygen sensor is about 4×10^{-4} m^2. The impingement rate is about 1 molecules per 10 second at oxygen partial pressure of ~10^{-25} atm. In comparison, at ambient condition, the impingement rate is ~ 10^{23} molecules/s. The slow kinetics of oxygen molecules drives the system away from thermodynamic equilibrium state. In experiment, however, the oxygen-sensor continuously monitors the oxygen partial pressure inside the annealing system and assumes thermodynamic equilibrium was achieved. Thus, the oxygen partial pressure measured by oxygen-sensor effectively represents the local near-surface and non-equilibrium value of P_{O2}. Because similar environment was experienced by both oxygen sensor and vanadium dioxide samples, we used such an effective value to characterize the low oxygen partial pressure environment near sample surface.

APPENDIX B: Zirconia-based oxygen sensor

Zirconia-based oxygen sensors are widely used for determining P_{O2} in a test gas at high temperatures as well as in automotive exhaust systems. The most common application is to measure the P_{O2} in exhaust gas in order to maintain an optimized air:fuel ratio [60]. Literature reports have also shown that this type of oxygen sensor is capable of measuring a P_{O2} as low as ~10^{-35} atm in an oxygen-poor gas environment [61].

Figure 8 shows a schematic of the zirconia-based oxygen sensor. The zirconia-based oxygen sensor is a potentiometric sensor. It consists of a tubular oxygen-ion-conducting zirconia electrolyte, and porous Pt anode and cathode. It is typically operated at a high temperature in the range of 500-800 °C to facilitate the chemical and electrochemical processes involved. In our work, the inside of the zirconia tube is exposed to air with a constant $P_{O2\,(air)}$ of 0.21 atm, while the outside to the test gas that has a much lower $P_{O2\,(Ar)}$. The same chemical species (oxygen) is present at both electrodes but at different partial pressures. Therefore, this oxygen sensor device is regarded as a concentration cell. Due to the difference in the oxygen partial pressure between air outside the chamber and Ar inside the chamber, the cell develops a voltage, which can be expressed as follows according to the Nernst equation [62, 63]:

$$E = \frac{RT}{4F}\ln\left(\frac{a_{O2\,(YSZ-Pt-air)}}{a_{O2(YSZ-Pt-Ar)}}\right) \qquad (4)$$

where E is the Nernst potential, R is the gas constant (8.31 J mol^{-1} K^{-1}, T is the operating temperature of the oxygen sensor (550 °C here), and F is the Faraday constant (96485 C mol^{-1}), $a_{O2(YSZ-Pt-air)}$ is the oxygen activity at the tripe phase boundary between YSZ (yttria-stabilized zirconia), Pt cathode, and air, and $a_{O2(YSZ-Pt-Ar)}$ is the oxygen activity at the tripe phase boundary between YSZ, Pt anode, and Ar. Under thermodynamic equilibrium condition, the oxygen activity at the YSZ-Pt-gas tripe phase boundary equals to the oxygen activity in the gas, which is expressed as the oxygen partial pressure in the gas divided by the standard pressure (1 atm). Therefore, the Nernst potential can be expressed as:

$$E = \frac{RT}{4F} \ln \left(\frac{P_{O2\,(air)}}{P_{O2(Ar)}} \right) \qquad (5)$$

where $P_{O2(air)}$ is the oxygen partial pressure in air (0.21 atm) and $P_{O2(Ar)}$ is the oxygen partial pressure of Ar inside the annealing system. By measuring the Nernst potential, the oxygen partial pressure inside the annealing system can be calculated by Equation (5).

In experiment, the Nernst relation is valid and enables us to measure the oxygen partial pressure inside the annealing system when the ionic conductivity is dominant over electronic conductivity for zirconia electrolyte, thus determining its dynamic range. For a typical zirconia electrolyte (8 mole percent yttria-stabilized zirconia), the ion, electron, and hole conductivities at 800 °C - 1050 °C and P_{O2} (0.21 – 10^{-17} atm), in ohm^{-1}cm^{-1}, were reported as [64]:

$$\sigma_{ion} = 1.63 \times 10^{2} \exp\left(-0.79 \frac{eV}{kT}\right) \qquad (6)$$

$$\sigma_{e} = 1.31 \times 10^{7} \exp\left(-3.88 \frac{eV}{kT}\right) P_{O2}^{-1/4} \qquad (7)$$

$$\sigma_{h} = 2.35 \times 10^{2} \exp\left(-1.67 \frac{eV}{kT}\right) P_{O2}^{+1/4} \qquad (8).$$

Based on these relations, ion, electron, and hole conductivities are calculated and shown in Fig. 9. With extrapolation of these relations in our measurement range (550 °C and 0.21 – 10^{-24} atm), the estimated ionic conductivity is more than 3 orders of magnitude higher than electron conductivity. This extrapolation to lower temperature is valid for zirconia since the electron contribution becomes less relevant with reducing temperature [64]. In addition, such a calculated result is also consistent with the reported experimental observations that the ionic conduction is dominant over 10^{-24} atm partial pressure range in stabilized zirconia [65]. Thus, in this work, we are still working within the dynamic range of zirconia-based oxygen sensors.

In this work, we measured the Nernst potential by Solartron 1287 electrochemical systems, which provides resolution of 10^{-5} V. The experimental Nernst potential (raw data) recorded during annealing is shown in Fig. 10. The noise on the recorded Nernst potential results from the fluctuation of local oxygen pressure near sensor surface and the noise from sensor and measurement system. It can be found in Fig. 10 that when the Mg-based trap is turned on, the Nernst potential increases from ~ 0.1 V to ~ 0.95 V. Such an increase in Nernst potential is much larger than the noise of signals, which therefore ensures the reliability of our measurement.

References

[1] S. V. Kalinin and N. A. Spaldin, Functional ion defects in transition metal oxides, Science **341**, 858 (2013).

[2] C. Wu, F. Feng, and Y. Xie, Design of vanadium oxide structures with controllable electrical properties for energy applications, Chem. Soc. Rev. **42**, 5157 (2013).

[3] J. Shi, Y. Zhou, and S. Ramanathan, Colossal resistance switching and band gap modulation in a perovskite nickelate by electron doping, Nat. Commun. **5**, 4860 (2014).

[4] K. Holman, T. McQueen, A. Williams, T. Klimczuk, P. Stephens, H. Zandbergen, Q. Xu, F. Ronning, and R. Cava, Insulator to correlated metal transition in $V_{1-x}Mo_xO_2$, Phys. Rev. B **79**, 245114 (2009).

[5] M. Marezio, D. B. McWhan, J. Remeika, and P. Dernier, Structural aspects of the metal-insulator transitions in Cr-doped VO_2, Phys. Rev. B **5**, 2541 (1972).

[6] C. Tang, P. Georgopoulos, M. Fine, J. Cohen, M. Nygren, G. Knapp, and A. Aldred, Local atomic and electronic arrangements in $W_xV_{1-x}O_2$, Phys. Rev. B **31**, 1000 (1985).

[7] Z. Yang, C. Ko, and S. Ramanathan, Oxide electronics utilizing ultrafast metal-insulator transitions, Ann. Rev. Mater. Res. **41**, 337 (2011).

[8] J. Rensberg, S. Zhang, Y. Zhou, A. S. McLeod, C. Schwarz, M. Goldflam, M. Liu, J. Kerbusch, R. Nawrodt, S. Ramanathan, D. N. Basov, F. Capasso, C. Ronning, and M. A. Kats, Active optical metasurfaces based on defect-engineered phase-transition materials, Nano Lett. **16**, 1050 (2016).

[9] M. A. Kats, R. Blanchard, S. Zhang, P. Genevet, C. Ko, S. Ramanathan, and F. Capasso, Vanadium dioxide as a natural disordered metamaterial: perfect thermal emission and large broadband negative differential thermal emittance, Phys. Rev. X **3**, 041004 (2013).

[10] T. Paik, S.-H. Hong, E. A. Gaulding, H. Caglayan, T. R. Gordon, N. Engheta, C. R. Kagan, and C. B. Murray, Solution-processed phase-change VO_2 metamaterials from colloidal vanadium oxide (VO_x) nanocrystals, ACS Nano **8**, 797 (2014).

[11] J. B. Goodenough, The two components of the crystallographic transition in VO_2, J. Solid State Chem. **3**, 490 (1971).

[12] R. M. Wentzcovitch, W. W. Schulz, and P. B. Allen, VO_2: Peierls or Mott-Hubbard? A view from band theory, Phys. Rev. Lett. **72**, 3389 (1994).

[13] F. J. Morin, Oxides which show a metal-to-insulator transition at the Neel temperature, Phys. Rev. Lett. **3**, 34 (1959).

[14] C. Weber, D. D. O'Regan, N. D. Hine, M. C. Payne, G. Kotliar, and P. B. Littlewood, Vanadium dioxide: A Peierls-Mott insulator stable against disorder, Phys. Rev. Lett. **108**, 256402 (2012).

[15] A. Zylbersztejn and N. F. Mott, Metal-insulator transition in vanadium dioxide, Phys. Rev. B **11**, 4383 (1975).

[16] M. M. Qazilbash, M. Brehm, B.-G. Chae, P.-C. Ho, G. O. Andreev, B.-J. Kim, S. J. Yun, A. V. Balatsky, M. B. Maple, F. Keilmann, H.-T. Kim, and D. N. Basov, Mott transition in VO_2 revealed by infrared spectroscopy and nano-imaging, Science **318**, 1750 (2007).

[17] M. Abbate, F. De Groot, J. Fuggle, Y. Ma, C. Chen, F. Sette, A. Fujimori, Y. Ueda, and K. Kosuge, Soft-x-ray-absorption studies of the electronic-structure changes through the VO_2 phase transition, Phys. Rev. B **43**, 7263 (1991).

[18] S. Biermann, A. Poteryaev, A. Lichtenstein, and A. Georges, Dynamical singlets and correlation-assisted Peierls transition in VO_2, Phys. Rev. Lett. **94**, 026404 (2005).

[19] M. Haverkort, Z. Hu, A. Tanaka, W. Reichelt, S. Streltsov, M. Korotin, V. Anisimov, H. Hsieh, H.-J. Lin, and C. Chen, Orbital-assisted metal-insulator transition in VO_2, Phys. Rev. Lett. **95**, 196404 (2005).

[20] J. Wei, H. Ji, W. Guo, A. H. Nevidomskyy, and D. Natelson, Hydrogen stabilization of metallic vanadium dioxide in single-crystal nanobeams, Nat. Nanotech. **7**, 357 (2012).

[21] N. B. Aetukuri, A. X. Gray, M. Drouard, M. Cossale, L. Gao, A. H. Reid, R. Kukreja, H. Ohldag, C. A. Jenkins, and E. Arenholz, Control of the metal-insulator transition in vanadium dioxide by modifying orbital occupancy, Nat. Phys. **9**, 661 (2013).

[22] M. Imada, A. Fujimori, and Y. Tokura, Metal-insulator transitions, Rev. Mod. Phys. **70**, 1039 (1998).

[23] J. G. Ramirez, T. Saerbeck, S. Wang, J. Trastoy, M. Malnou, J. Lesueur, J.-P. Crocombette, J. E. Villegas, and I. K. Schuller, Effect of disorder on the metal-insulator transition of vanadium oxides: Local versus global effects, Phys. Rev. B **91**, 205123 (2015).

[24] V. Andreev, V. Klimov, and M. Kompan, Influence of hydrogenation on electrical conductivity of vanadium dioxide thin films, Phys. Solid State **54**, 601 (2012).

[25] Z. Yang, Y. Zhou, and S. Ramanathan, Studies on room-temperature electric-field effect in ionic-liquid gated VO_2 three-terminal devices, J. Appl. Phys. **111**, 014506 (2012).

[26] J. Jeong, N. Aetukuri, T. Graf, T. D. Schladt, M. G. Samant, and S. S. Parkin, Suppression of metal-insulator transition in VO_2 by electric field–induced oxygen vacancy formation, Science **339**, 1402 (2013).

[27] M. Nakano, K. Shibuya, D. Okuyama, T. Hatano, S. Ono, M. Kawasaki, Y. Iwasa, and Y. Tokura, Collective bulk carrier delocalization driven by electrostatic surface charge accumulation, Nature **487**, 459 (2012).

[28] Y. Zhou and S. Ramanathan, Relaxation dynamics of ionic liquid—VO_2 interfaces and influence in electric double-layer transistors, J. Appl. Phys. **111**, 084508 (2012).

[29] H. Ji, J. Wei, and D. Natelson, Modulation of the electrical properties of VO2 nanobeams using an ionic liquid as a gating medium, Nano Lett. **12**, 2988 (2012).

[30] X. Peng, Y. Yang, Y. Hou, H. C. Travaglini, L. Hellwig, S. Hihath, K. van Benthem, K. Lee, W. Liu, and D. Yu, Efficient and hysteresis-free field effect modulation of ambipolarly doped vanadium dioxide nanowires, Phys. Rev. Appl. **5**, 054008 (2016).

[31] M. Goldflam, M. Liu, B. Chapler, H. Stinson, A. Sternbach, A. McLeod, J. Zhang, K. Geng, M. Royal, and B.-J. Kim, Voltage switching of a VO_2 memory metasurface using ionic gel, Appl. Phys. Lett. **105**, 041117 (2014).

[32] C. Griffiths and H. Eastwood, Influence of stoichiometry on the metal□semiconductor transition in vanadium dioxide, J. Appl. Phys. 45, 2201 (1974).

[33] H.-T. Zhang, L. Zhang, D. Mukherjee, Y.-X. Zheng, R. C. Haislmaier, N. Alem, and R. Engel-Herbert, Wafer-scale growth of VO_2 thin films using a combinatorial approach, Nat. Commun. **6**, 8475 (2015).

[34] D. Ruzmetov, S. D. Senanayake, V. Narayanamurti, and S. Ramanathan, Correlation between metal-insulator transition characteristics and electronic structure changes in vanadium oxide thin films, Phys. Rev. B **77**, 195442 (2008).

[35] T. Katsura and M. Hasegawa, Equilibria in the V_2O_3-VO_2 system at 1600° K, Bull. Chem. Soc. Jpn **40**, 561 (1967).

[36] S. Zhang, I. S. Kim, and L. J. Lauhon, Stoichiometry engineering of monoclinic to rutile phase transition in suspended single crystalline vanadium dioxide nanobeams, Nano Lett. **11**, 1443 (2011).

[37] See Supplemental Material at [] for [thermodynamic analysis of stability of vanadium dioxide and sapphire substrate at low oxygen partial pressures, ellipsometry data and model fitting of vanadium dioxide after annealing, annealing of 100 nm PVD-grown vanadium dioxide film at low oxygen partial pressure, stability of vanadium dioxide after annealing at ambient condition, annealing of vanadium dioxide at low oxygen partial pressure over multiple cycles, and Off - axis XRD studies on vanadium dioxide after annealing].

[38] E. Hryha, E. Rutqvist, and L. Nyborg, Stoichiometric vanadium oxides studied by XPS, Surf. Interface Anal. **44**, 1022 (2012).

[39] D. D. S. Meneses, M. Malki, and P. Echegut, Structure and lattice dynamics of binary lead silicate glasses investigated by infrared spectroscopy, J. Non-cryst. Solids **352**, 769 (2006).

[40] T. E. Tiwald, D. W. Thompson, J. A. Woollam, W. Paulson, and R. Hance, Application of IR variable angle spectroscopic ellipsometry to the determination of free carrier concentration depth profiles, Thin Solid Films **313**, 661 (1998).

[41] J. Wei, Z. Wang, W. Chen, and D. H. Cobden, New aspects of the metal–insulator transition in single-domain vanadium dioxide nanobeams, Nat. Nanotech. **4**, 420 (2009).

[42] F. Gervais and B. Piriou, Anharmonicity in several-polar-mode crystals: adjusting phonon self-energy of LO and TO modes in Al_2O_3 and TiO_2 to fit infrared reflectivity, J. Phys. C: Solid State Phys. **7**, 2374 (1974).

[43] M. Qazilbash, K. Burch, D. Whisler, D. Shrekenhamer, B. Chae, H. Kim, and D. Basov, Correlated metallic state of vanadium dioxide, Phys. Rev. B **74**, 205118 (2006).

[44] F. J. Wong, Y. Zhou, and S. Ramanathan, Epitaxial variants of VO_2 thin films on complex oxide single crystal substrates with 3m surface symmetry, J. Crys. Growth **364**, 74 (2013).

[45] K. Rogers, An X-ray diffraction study of semiconductor and metallic vanadium dioxide, Powder Diffr. **8**, 240 (1993).

[46] S. Kachi, K. Kosuge, and H. Okinaka, Metal-insulator transition in V_nO_{2n-1}, J. Solid State Chem. **6**, 258 (1973).

[47] G. Silversmit, D. Depla, H. Poelman, G. B. Marin, and R. De Gryse, Determination of the V2p XPS binding energies for different vanadium oxidation states (V5+ to V0+), J. Electron Spectrosc. Relat. Phenom. **135**, 167 (2004).

[48] K. Shibuya, M. Kawasaki, and Y. Tokura, Metal-insulator transition in epitaxial $V_{1-x}W_xO_2$ ($0\leq x\leq 0.33$) thin films, Appl. Phys. Lett. **96**, 022102 (2010).

[49] H. Takami, T. Kanki, S. Ueda, K. Kobayashi, and H. Tanaka, Electronic structure of W-doped VO_2 thin films with giant metal–insulator transition investigated by hard X-ray core-level photoemission spectroscopy, Appl. Phys. Exp. **3**, 063201 (2010).

[50] R. Srivastava and L. Chase, Raman spectrum of semiconducting and metallic VO_2, Phys. Rev. Lett. **27**, 727 (1971).

[51] P. Schilbe and D. Maurer, Lattice dynamics in VO_2 near the metal-insulator transition, Mater. Sci. Eng. A **370**, 449 (2004).

[52] H.-T. Kim, B.-G. Chae, D.-H. Youn, G. Kim, K.-Y. Kang, S.-J. Lee, K. Kim, and Y.-S. Lim, Raman study of electric-field-induced first-order metal-insulator transition in VO_2-based devices, Appl. Phys. Lett. **86**, 242101 (2005).

[53] J. M. Atkin, S. Berweger, E. K. Chavez, M. B. Raschke, J. Cao, W. Fan, and J. Wu, Strain and temperature dependence of the insulating phases of VO_2 near the metal-insulator transition, Phys. Rev. B **85**, 020101 (2012).

[54] J. D. Budai, J. Hong, M. E. Manley, E. D. Specht, C. W. Li, J. Z. Tischler, D. L. Abernathy, A. H. Said, B. M. Leu, and L. A. Boatner, Metallization of vanadium dioxide driven by large phonon entropy, Nature **515**, 535 (2014).

[55] M. M. Qazilbash, A. Schafgans, K. Burch, S. Yun, B. Chae, B. Kim, H.-T. Kim, and D. Basov, Electrodynamics of the vanadium oxides VO_2 and V_2O_3, Phys. Rev. B **77**, 115121 (2008).

[56] A. Cavalleri, M. Rini, H. Chong, S. Fourmaux, T. Glover, P. Heimann, J. Kieffer, and R. Schoenlein, Band-selective measurements of electron dynamics in VO_2 using femtosecond near-edge X-ray absorption, Phys. Rev. Lett. **95**, 067405 (2005).

[57] A. Roine, *HSC Chemistry Database 5.11,* (Outokumpu Research, Finland, 2002).

[58] E. Jud, M. Tang, and Y.-M. Chiang, Stability of $HfO_2/SiO_x/Si$ surficial films at ultralow oxygen activity, J. Appl. Phys. **103**, 4108 (2008).

[59] N. Marquardt, Introduction to the principles of vacuum physics, Cern. Eur. Organ. Nucl. Res. 1 (1999).

[60] R. Ramamoorthy, P. Dutta, and S. Akbar, Oxygen sensors: materials, methods, designs and applications, J. Mater.Sci. **38**, 4271 (2003).

[61] A. Inoishi, Y.-W. Ju, S. Ida, and T. Ishihara, Mg–air oxygen shuttle batteries using a ZrO 2-based oxide ion-conducting electrolyte, Chem. Commun. **49**, 4691 (2013).

[62] A. J. Bard and L. Faulkner, *Electrochemical methods: principles and applications*, (2nd edition, Wiley New York, 2001).

[63] R. O'hayre, S.-W. Cha, F. B. Prinz, and W. Colella, *Fuel cell fundamentals*, (John Wiley & Sons, 2016).

[64] J. H. Park and R. N. Blumenthal, Electronic Transport in 8 Mole Percent Y_2O_3-ZrO_2, J. Electrochem. Soc. **136**, 2867 (1989).

[65] N. Q. Minh, Ceramic fuel cells, J. Am. Ceram. Soc. **76**, 563 (1993).

Figure 1

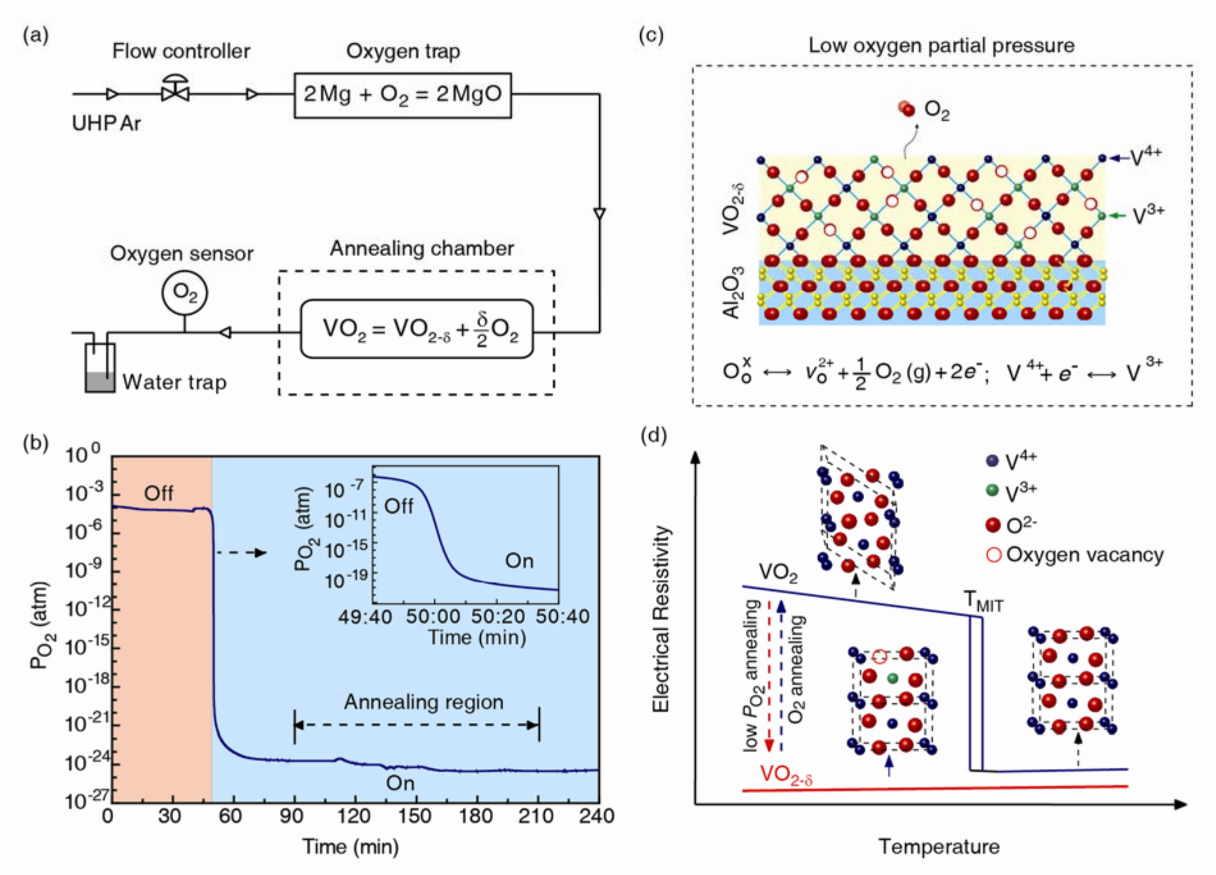

FIG. 1. Metallization of vanadium dioxide at extremely low oxygen partial pressure. (a) Experimental setup for annealing VO_2 at low oxygen partial pressure. (b) Real-time oxygen partial pressure monitored by a zirconia-based oxygen sensor, where pristine VO_2 was annealed at $P_{O2} \sim 10^{-24}$ atm. The inset shows the P_{O2} in a narrow time window. (c) At low oxygen partial pressure, oxygen vacancies are created in VO_2, and the oxidization state of vanadium is reduced from V^{4+} to V^{3+}. (d) By introducing a high concentration of oxygen vacancies, the metal-insulator transition is suppressed and a metallic non-volatile $VO_{2-\delta}$ state is observed down to very low temperatures. The process can be reversed by oxygen annealing.

Figure 2

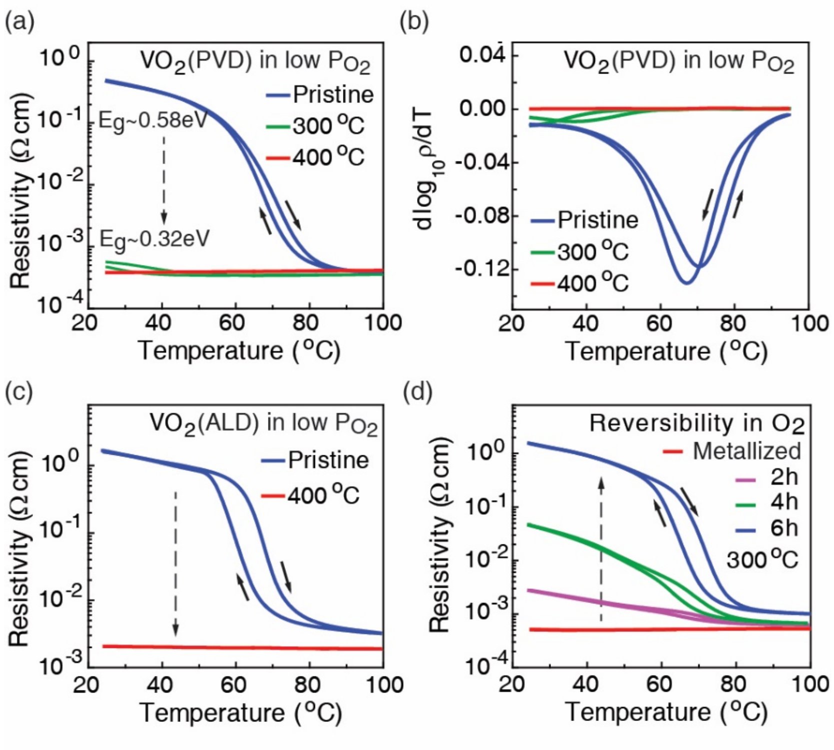

FIG. 2. Manipulation of electrical properties of VO_2 thin films after annealing at $P_{O2} \sim 10^{-24}$ atm. (a) Resistivity-temperature curves of 40 nm PVD-grown VO_2 annealed at 300°C and 400 °C, respectively, for 2 hours. After annealing, the thin films show metallic behavior down to room temperature. (b) Corresponding derivative of the resistivity-temperature curve, for various annealing conditions. (c) Resistivity-temperature curves of 40 nm ALD-grown VO_2 annealed at 400 °C for 2 hours. The metallization behavior of VO_2 under low oxygen partial pressure is reproducible with ALD-grown films. (d) After metallization of 40 nm PVD-grown VO_2 at low P_{O2} for 400 °C 2 hours in (a), the sample was further annealed in pure oxygen at 300 °C for 2 hours, 4 hours, and 6 hours. The resistivity-temperature curves show that the metal-insulator transition is recovered after annealing in oxygen.

Figure 3

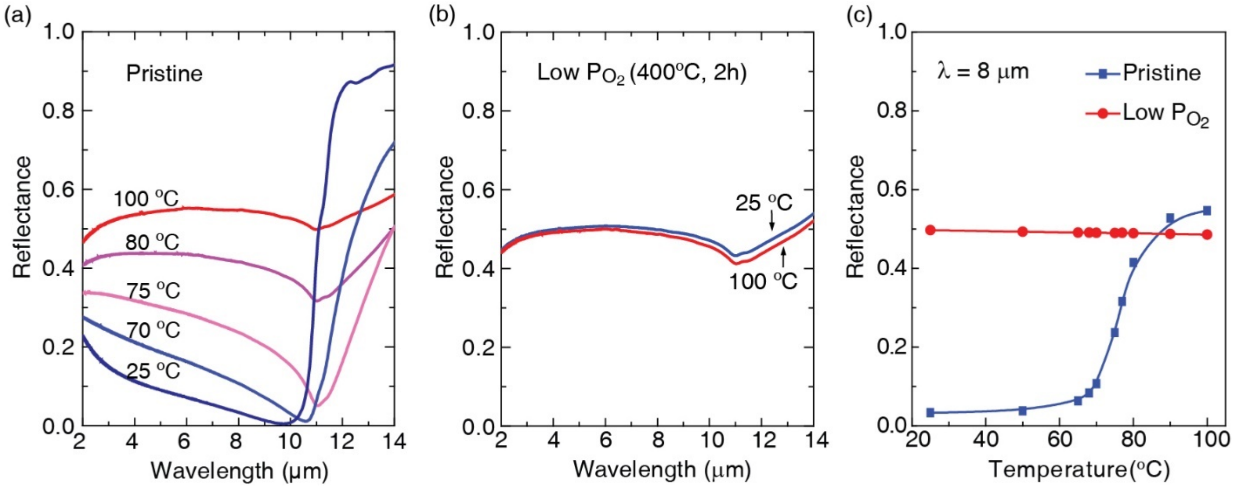

FIG. 3. Mid-IR reflectance of VO_2 before and after annealing at P_{O2} ~ 10^{-24} atm. (a) Temperature-dependent reflectance spectrum of pristine VO_2 deposited on a sapphire substrate. After annealing at P_{O2} ~ 10^{-24} atm at 400 °C for 2 hours, the reflectance spectrum of the sample is shown in (b), where weak temperature-dependent behavior is observed. The sample maintains a high reflectance when cooled, demonstrating the vanishing of metal-insulator transition after annealing. (c) Single-wavelength ($\lambda = 8$ μm) temperature-dependent reflectance of VO_2 after annealing at low oxygen partial pressure at 400 °C for 2 hours. The reflectance of the pristine sample increases sharply when heated past the metal-insulator transition temperature. After annealing at low oxygen partial pressure, the sample shows high reflectance, similar to that of the thermally induced metallic state of the pristine sample. Moreover, the reflectance of the annealed sample decreases slightly with heating, indicative of metallic behavior.

Figure 4

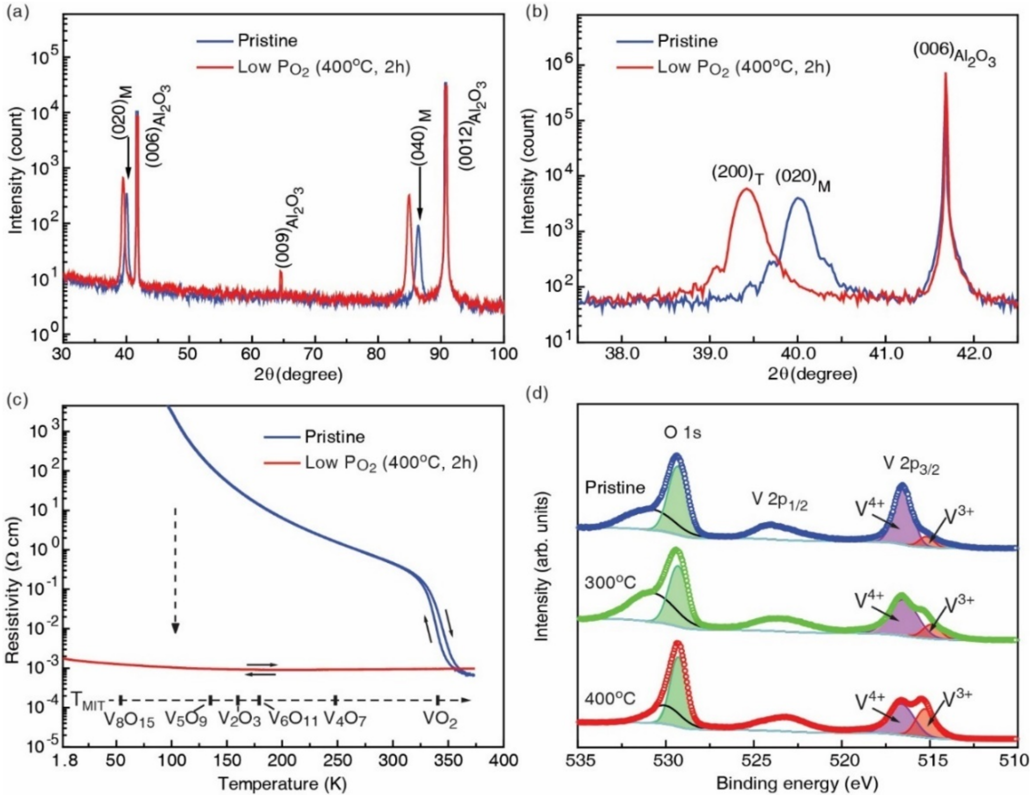

FIG. 4. XRD curves of pristine and annealed VO_2 thin films (a) over a wide range of angles and (b) around the $(020)_M$ peak. The shifting of the $(020)_M$ peak to the $(200)_T$ peak demonstrates that the high-temperature tetragonal (rutile) structure is maintained down to room temperature after annealing. (c) The resistivity of annealed thin films is measured down to 1.8 K. The metal-insulator transition temperatures of various Magnéli phases are depicted. The flat resistivity-temperature curve over the entire temperature range indicates the absence of Magnéli phases in the oxygen deficient $VO_{2-\delta}$ thin films. (d) XPS analysis of pristine and annealed thin films. The shifting of V 2p1/2 to lower binding energy and the appearance of V^{3+} $2p_{3/2}$ photoemission indicate the strong reduction of the oxidization state of the vanadium ion under oxygen deficiency. The estimated oxygen vacancy level of the annealed sample $VO_{2-\delta}$ is $\delta = 0.08$ at 300 ^{o}C and $\delta = 0.2$ at 400 ^{o}C.

Figure 5

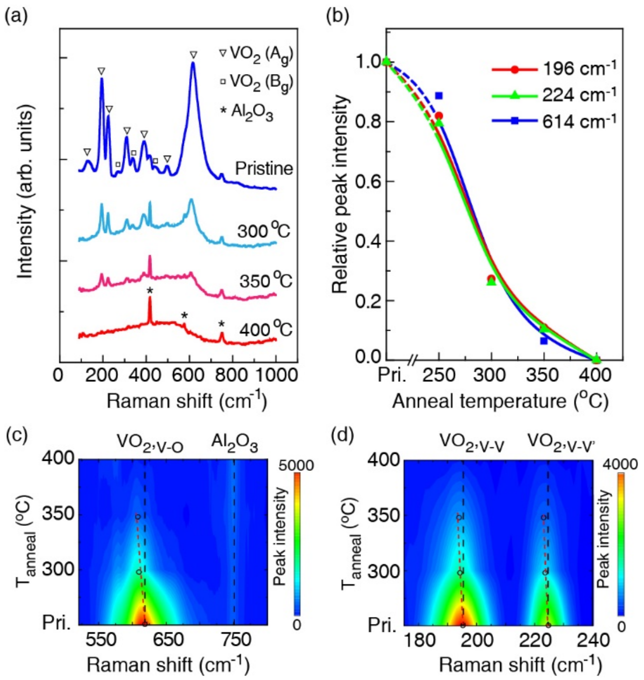

FIG. 5. Room temperature Raman spectra of VO_2 after annealing at $P_{O2} \sim 10^{-24}$ atm. (a) Raman spectra of PVD-grown 40 nm VO_2 annealed at 300 °C, 350 °C, and 400 °C for 2 hours. For the pristine sample, Raman peaks corresponding to the monoclinic structure appear at 129, 196, 224, 308, 386, 498, and 614 cm^{-1} for A_g symmetry, and 268, 340, and 445 cm^{-1} for B_g symmetry. For the sample annealed at 400 °C, the heavily damped Raman peak at 530 cm^{-1} corresponds to the A_{1g} mode of the rutile structure. Peaks at 421, 575, and 751 cm^{-1} result from Raman scattering of the Al_2O_3 substrate. (b) Relative intensity of the Raman peaks at 196, 224, and 614 cm^{-1} as a function of the annealing temperature. (c) The A_g mode at 614 cm^{-1} as a function of the annealing temperature. This Raman mode is related to V-O bonding of VO_2. (d) The A_g modes at 196 and 224 cm^{-1} as a function of the annealing temperature. These Raman modes are related to V-V bonding and tilting of VO_2. Softening of the Raman modes, V-O bonding (c) and V-V bonding (d), occurs with the increase of the annealing temperature, demonstrating the instability of monoclinic structure upon the introduction of oxygen vacancies.

Figure 6

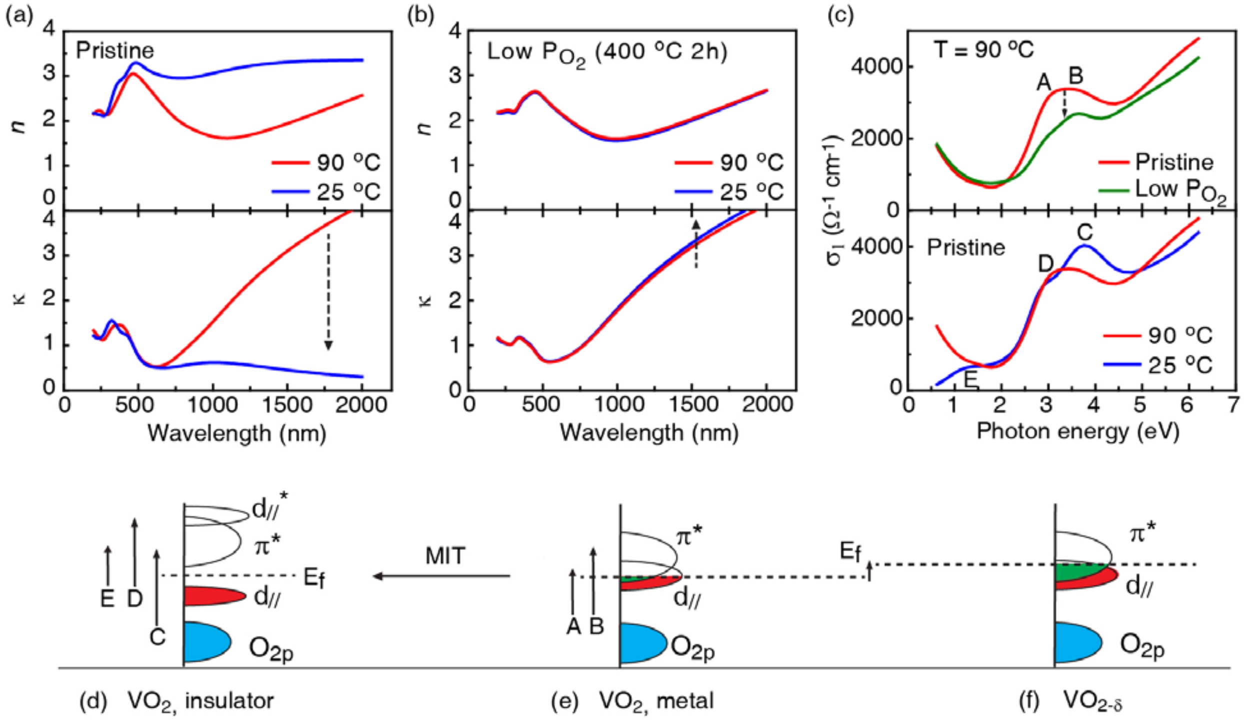

FIG. 6. Optical properties of VO_2 before and after annealing at P_{O2} ~ 10^{-24} atm. (a) Real (n) and imaginary (κ) parts of the complex refractive index of pristine VO_2 at 25°C and 90°C, below and above its metal-insulator transition temperature. After annealing at P_{O2} ~ 10^{-24} atm, the complex refractive index of oxygen deficient $VO_{2-\delta}$ at 25°C and 90°C is shown in (b), where Drude-like metallic behavior is observed and no phase transition occurs. (c) Comparison of the optical conductivity between the thermally induced metallic state of pristine VO_2 and the oxygen-deficiency-induced metallic state of $VO_{2-\delta}$ at 90 °C. The optical conductivity of pristine VO_2 across the thermally induced metal-insulator transition is shown in lower panel. (d)-(f) Schematic illustration of the band structure of pristine VO_2 in insulating state (d) and metallic state (e), while the band structure of oxygen deficiency $VO_{2-\delta}$ is shown in (f), where strong charge filling in the π^* and $d_{//}$ orbitals occurs.

Figure 7

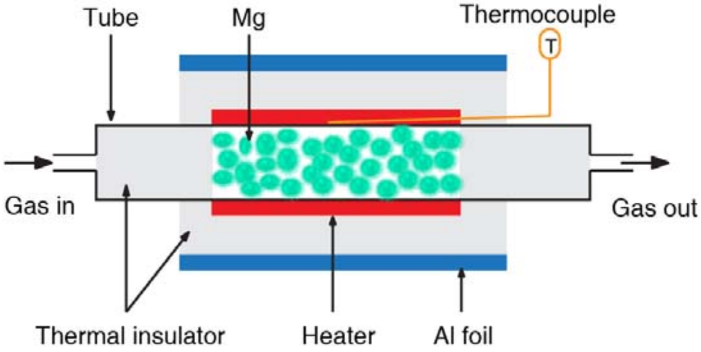

FIG. 7. Schematic of the Mg-based oxygen trap for achieving ultra-low oxygen partial pressure.

Figure 8

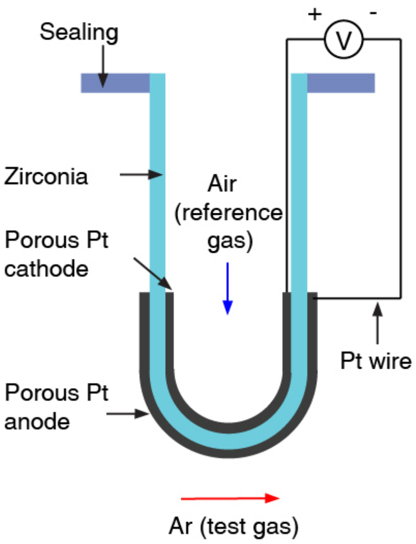

FIG. 8. Schematic of the zirconia-based oxygen sensor.

Figure 9

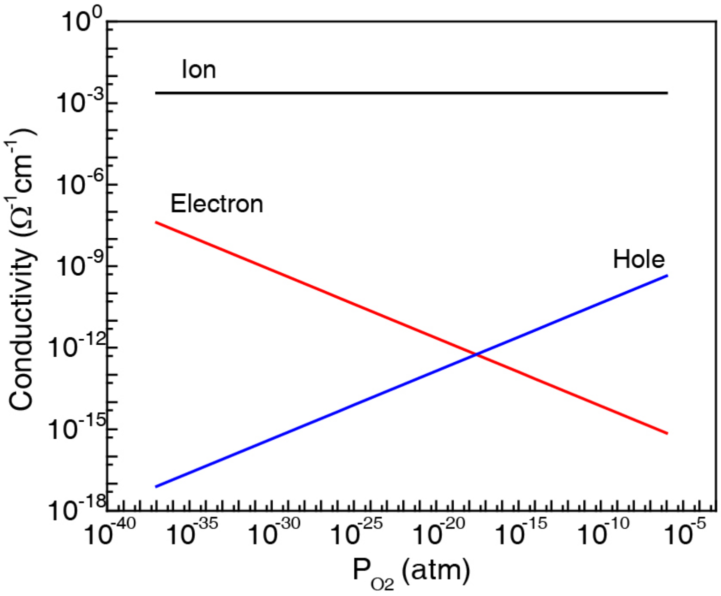

FIG. 9. Ion, electron, and hole conductivity of zirconia at 550 °C calculated based on Equations (6) – (8).

Figure 10

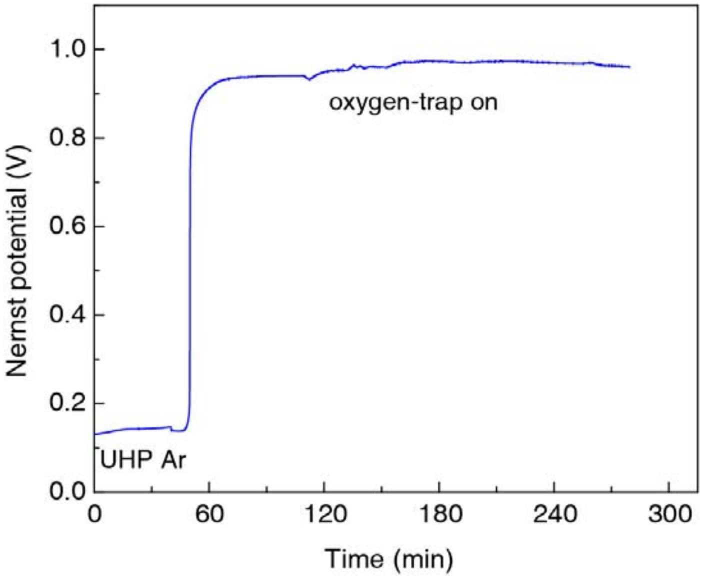

FIG. 10. The experimental Nernst potential measured during low oxygen partial pressure annealing.

TABLE I. Calculated equilibrium constant (K_{eq}) of $Mg + ½ O_2(g) = MgO$.

Temperature (°C)	K_{eq}
350	3.83×10^{89}
400	1.26×10^{82}
450	4.49×10^{75}
500	1.10×10^{70}